

Effects of forcing geometry on two-dimensional weak turbulence

Yang Liao, Douglas H. Kelley, and Nicholas T. Ouellette*

Department of Mechanical Engineering & Materials Science, Yale University, New Haven, Connecticut 06520, USA

(Received 1 May 2012; published 10 September 2012)

Using high-resolution particle tracking velocimetry, we study the effects of the forcing geometry on the statistics of an electromagnetically stirred thin-layer flow. We consider two forcing arrangements: one that produces a lattice of vortices as a base flow, and one that produces an array of shear bands. We find that the vortex flow drives stronger fluctuating kinetic energy while the shear-band flow leads to more intense fluctuating velocity gradients. We explain our results by considering the spectral flow of energy in the system. Our results have implications for the design of two-dimensional flow experiments.

DOI: [10.1103/PhysRevE.86.036306](https://doi.org/10.1103/PhysRevE.86.036306)

PACS number(s): 47.20.Ky, 47.27.-i

I. INTRODUCTION

Many large-scale geophysical flows can to a degree be approximated as two-dimensional (2D) [1,2]. Although at small scales flows in the atmosphere and oceans are undeniably 3D, their lateral extent is so much larger than their depth that (with the added effects of planetary rotation and density stratification) large-scale motion lies primarily in the plane. This observation has motivated the development of 2D fluid mechanics, and particularly of 2D turbulence, via theory and modeling, computational studies, and laboratory work. But even though experimental 2D fluid mechanics is developing rapidly, the understanding of the quirks of typical experimental systems is not as well developed as it is for standard 3D flows [2].

Two dominant systems have emerged for studying 2D turbulence in the laboratory: thin layers of electrolytic fluid that are stirred by electromagnetic Lorentz forces and soap films that flow under gravity [2]. Soap films are the 2D analog of wind tunnels. They typically have a mean flow that is large compared to the turbulent fluctuations, and the turbulence is advected downstream. In contrast, electromagnetic thin-layer flows are closer in spirit to the zero-mean-flow turbulence generators such as von Kármán swirling flows and oscillating grid systems that have been well studied in recent years for 3D turbulence [3]. Turbulence is driven in soap films by running the film through a comb, which plays the role of the grid in a wind tunnel. In an electromagnetic thin-layer flow, an electric current is driven through the (electrolytic) fluid, which itself lies above an array of magnets; the current and magnets together produce Lorentz body forces that stir the fluid. Intrinsic flow instabilities excite the turbulent fluctuations.

Because of the tendency of 2D flows to transfer energy from the injection scale to larger length scales [4–6], the details of the forcing may matter more in 2D systems than they do in 3D turbulence. Here, we study how the layout of the magnets (and therefore the geometry of the forcing) in an electromagnetic thin-layer system affects the flow field. We consider two magnet arrangements: a checkerboard pattern (producing a vortex lattice at low Reynolds number) and parallel stripes (producing parallel shear bands at low Reynolds number). We show that the magnet layout does indeed affect the velocity

statistics. The vortex flow tends to produce stronger velocity fluctuations, while the shear flow leads to stronger velocity gradients. We interpret these results in terms of the symmetries of the forcing and the spectral transfer of energy in the flows. Thus, depending on what one wants to study, different magnet layouts will be appropriate.

We begin in Sec. II by describing our apparatus and experimental methods in detail. Then, in Sec. III, we present our results. We measure how the injected energy is distributed between the mean flow and the velocity fluctuations, and how the gradient statistics depend on the magnet layout. We also show how the transfer of energy between length scales changes in the two flows. Finally, in Sec. IV, we summarize our findings and draw conclusions.

II. EXPERIMENTAL METHODS

A. Apparatus

Our experimental apparatus, sketched in Fig. 1 and described in detail elsewhere [7], is similar to other electromagnetic thin-layer flows [8–13], though it is larger than many. The lateral size of the driven area measures 86 cm \times 86 cm. The working fluid is a solution of 16% by mass NaCl in water, with a density of $\rho = 1116$ kg/m³ and a kinematic viscosity of $\nu = 1.24 \times 10^{-6}$ m²/s. The depth of this layer was approximately 5 mm. A second layer of pure water (also 5 mm deep) lies above the electrolyte to provide an interface with vanishing surface tension on which we float tracer particles to measure the flow field. The electrolyte sits on top of a glass bottom plate; beneath the glass is a square 34 \times 34 grid of neodymium-iron-boron (NdFeB) grade N52 magnets, spaced 2.54 cm on center. Each magnet is cylindrical, with a diameter of 12.7 mm, a thickness of 3.2 mm, and a peak magnetic field of about 0.3 T [14]. By passing a steady electrical current through the electrolyte, we produce steady Lorentz forces in the bulk of the fluid and cause it to flow. By varying the magnitude of the current, we can vary the bulk Reynolds number $Re = UL_f/\nu$, where $L_f = 2.54$ cm is the center-to-center magnet separation distance and U is the measured root-mean-square velocity. As long as the Reynolds number is not too large (below about 200 for our apparatus), the flow is nearly entirely in the plane and is 2D [7]. We note that this Reynolds number is essentially a nondimensional measure of the strength of the electric current, since the magnet spacing L_f , the kinematic viscosity, and the

*nicholas.ouellette@yale.edu

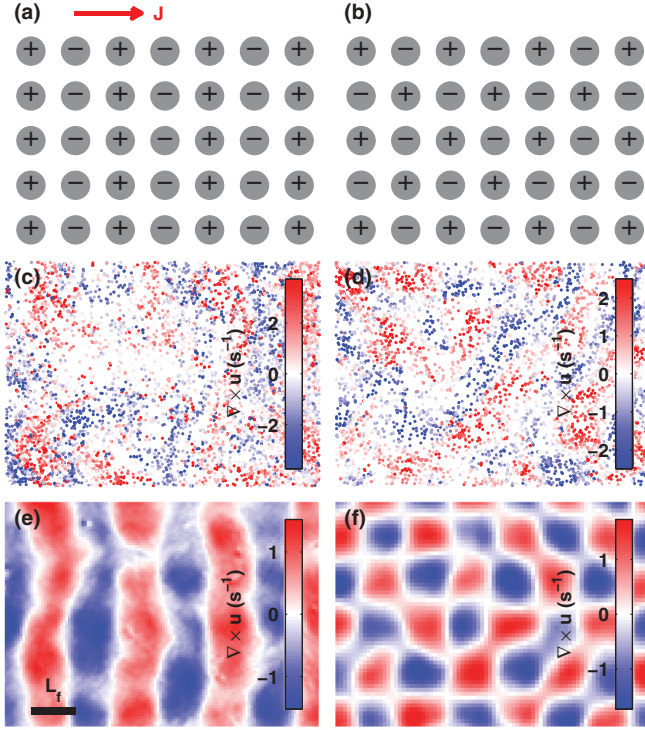


FIG. 1. (Color online) Forcing geometry and typical flow fields. Magnets are arranged (a) with polarity alternating in one-dimensional rows for shear-band flow, or (b) in two dimensions like a checkerboard for vortex flow. Here + and – indicate the magnetic field direction. A forcing current \mathbf{J} flows in the \hat{x} direction; when it is large, instantaneous flow fields (here represented with vorticity) are apparently disordered in both (c) shear-band flow and (d) vortex flow. Here each dot is one tracked particle, and its color indicates its vorticity $\nabla \times \mathbf{u}$. The influence of the underlying forcing geometry is apparent in an ensemble average of flow fields in (e) shear-band flow and (f) vortex flow. Color indicates vorticity. All panels show the same field of view, about 30% of the measurement region and about 3% of the fluid surface.

magnetic field are all fixed and we vary the velocity only by changing the current [14].

Our magnets always lie on a square grid, but their polarities can be changed to vary the flow structure. As shown in Fig. 1, we have studied two configurations: stripes of magnets, which produce shear bands at low Reynolds number, and an alternating checkerboard pattern, which produces a vortex lattice. The stripes inject energy into the flow at a length scale that is well defined in only one direction, whereas the checkerboard injects energy at a length scale that is well defined in both directions. At high Reynolds number, instantaneous flow fields appear disordered for both configurations. Nevertheless, the statistical signature of the underlying forcing geometry remains and is apparent in time-averaged mean flow fields (also shown in Fig. 1).

B. Particle tracking

We measure the flow quantitatively using particle tracking velocimetry (PTV). We seed the flow with small (51 μm diameter) fluorescent polystyrene spheres. With a specific

gravity of 1.05, these tracer particles float at the interface between the salty layer and the pure water layer; since this interface does not have a bulk surface tension, there are no long-range forces coupling the particles. We illuminate the particles with blue light-emitting diodes, and record their green fluorescence from above with a 4 megapixel camera at a rate of 60 frames per second. We process the movies and construct particle trajectories using a predictive tracking method described in detail elsewhere [15].

In the present study, we perform experiments at statistically steady conditions, allowing the flow to stabilize before recording data. We then track roughly 30 000 particles per frame for 5000 frames (between 3 and 37 eddy turnover times, depending on the Reynolds number) in each experiment, ensuring that the flow field is well sampled in space and time. We compute particle velocities by convolving the measured trajectories with a Gaussian smoothing and differentiating kernel [16].

C. Velocity field conditioning

Despite taking care to minimize any forcing or flow in the depth direction, some residual three-dimensionality will always remain in any physical apparatus due to effects such as Ekman pumping [7]. Thus, we post-process our velocity field data in order to remove the (small) third component of the velocity.

Since we observe our particles only in a single plane, we cannot directly measure the third component of the field. But any flow in the depth direction will be manifest in the in-plane velocity field as an apparent compressibility. This component of the field can be removed via a Helmholtz decomposition [17], since any vector field that vanishes at its boundary (which may be at infinity) can be uniquely decomposed into a compressible component and a rotational component. In two dimensions, the measured velocity field can be written as

$$\mathbf{u}_{\text{meas}} = \nabla \Phi - \hat{z} \times \nabla \Psi, \quad (1)$$

where

$$\nabla = \hat{x} \frac{\partial}{\partial x} + \hat{y} \frac{\partial}{\partial y}. \quad (2)$$

Since \mathbf{u}_{meas} is a velocity field, Φ is the velocity potential and Ψ is the stream function. The first term on the right-hand side of Eq. (1) is irrotational in two dimensions, and the second is solenoidal; that is,

$$\nabla \times (\nabla \Phi) = 0, \quad (3)$$

and

$$\nabla \cdot (\hat{z} \times \nabla \Psi) = 0. \quad (4)$$

Removing the irrotational (compressible) component of the measured 2D velocity field will leave a field \mathbf{u} free of apparent compressibility and therefore free of out-of-plane motion.

Our velocity fields, however, do not vanish at the boundary of our measurement region since we measure only the central 10% of the flow in order to avoid edge effects. Thus, our effective boundaries are open because $|\mathbf{u}| \neq 0$ at the edge of the field of view. With open boundaries, decomposition into incompressible and irrotational components remains possible but is no longer unique due to a possible harmonic component

that is both solenoidal *and* irrotational and can therefore be assigned to either term in Eq. (1) [18]. We seek flow fields that are incompressible in the plane but contain as much of the measured energy as possible, so we assign the harmonic component to the second (incompressible) term in Eq. (1). To do this, we solve the Poisson equation

$$\nabla^2 \Phi = \nabla \cdot \mathbf{u}_{\text{meas}} \quad (5)$$

for the minimal velocity potential, subject to the condition that it vanishes at the boundary. We solve this equation numerically using finite-element tools that allow gradient calculations at the particle locations and do not require imposing an arbitrary grid. Once Φ is known, we calculate the compressible component of the flow and subtract it from our measurements to obtain the incompressible velocity field

$$\mathbf{u} = \mathbf{u}_{\text{meas}} - \nabla \Phi. \quad (6)$$

For all data shown below, the energy associated with $\nabla \Phi$ is less than 4% of the total flow energy.

We note that one can also remove apparent compressibility via a least-squares projection of \mathbf{u}_{meas} onto a set of incompressible basis functions [7]. Although this projection method is highly accurate, it can be very computationally expensive, especially for large numbers of tracer particles. The Helmholtz decomposition method described here is much faster, and is sufficiently accurate for our purposes.

Finally, as shown in Fig. 1, we Reynolds-decompose our measured flow fields, splitting them into a mean component, computed as the time average of the instantaneous velocity fields, and a fluctuation around this mean. Note that the mean flow fields are not uniform or isotropic for either magnet arrangement. We show the velocity statistics of the mean and fluctuating components for both flows in Fig. 2.

III. RESULTS AND DISCUSSION

A. Energy

Turbulent flow requires large velocity *fluctuations*; large velocity alone does not lead to developed turbulence. Measuring how much of the injected energy goes towards producing mean flow versus how much drives fluctuations for different forcing configurations can thus give us insight into how the forcing affects the efficiency of generating turbulence.

To this end, we plot in Fig. 3 the mean kinetic energy per unit mass $\langle E \rangle = \langle u^2 \rangle / 2$, where the average is taken over space and time, in both the mean flow and the fluctuations as a function of Reynolds number for our two flows. The error bars here and below are computed from the statistical variation between the averages of subsets of our full data sets. In all cases, $\langle E \rangle$ increases with Re , as it must given our definition of Re . But the partitioning of energy between the mean flow and the fluctuations is not the same for the two flows we consider. The energy injected into the mean flow is smaller for the vortex flow than it is for the shear-band flow at all Re ; the opposite effect is present (though weakly) for the energy in the fluctuating component of the velocity field. Thus, the vortex flow is slightly more efficient at generating velocity fluctuations than the shear-band flow is.

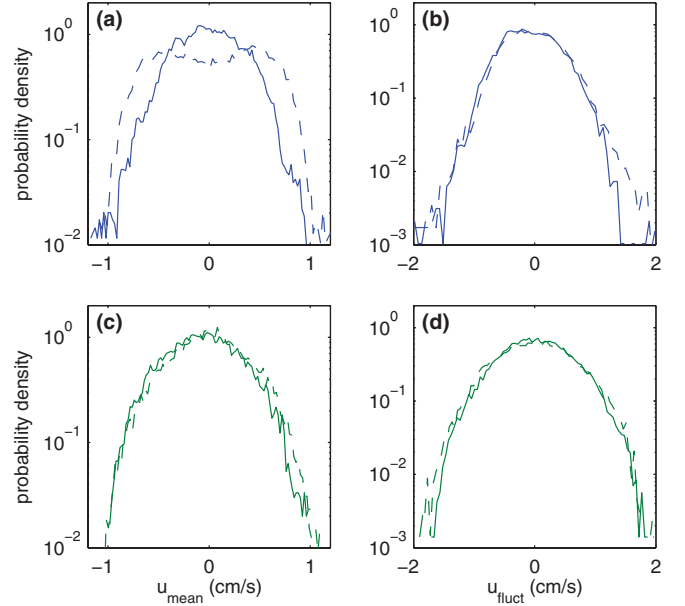


FIG. 2. (Color online) Distributions of velocity components for (a) mean flow in the shear-band flow, (b) fluctuations in the shear-band flow, (c) mean flow in the vortex flow, and (d) fluctuations in the vortex flow. Solid lines show distributions of $\mathbf{u} \cdot \hat{x}$, and dashed lines show distributions of $\mathbf{u} \cdot \hat{y}$. The distributions come from experiments with $\text{Re} = 243$ (shear-band flow) and $\text{Re} = 244$ (vortex flow). The shear bands themselves flow along the \hat{y} direction, as is evident from the bimodal distribution of its mean flow.

B. Velocity gradients

Energy, however, is not the only quantity of interest in complex flow. In many cases, we desire a flow with strong velocity gradients. We therefore also measured the velocity gradients, again separating them into their mean and fluctuating components.

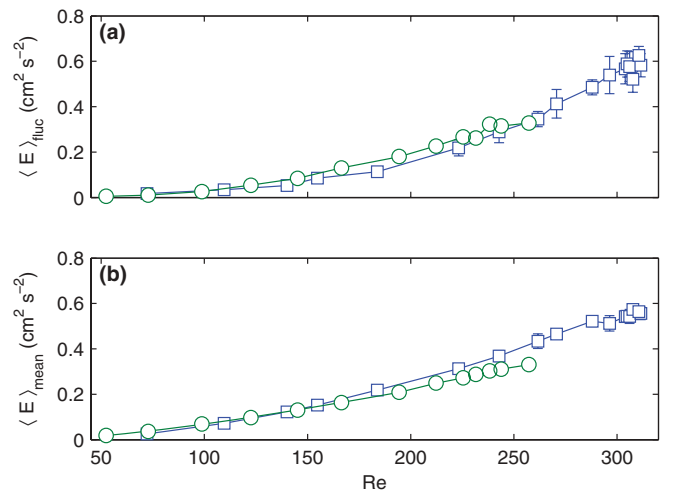


FIG. 3. (Color online) Average kinetic energy $\langle E \rangle$ for the (a) fluctuating and (b) mean components of the flow field as a function of Reynolds number. Data are shown for the vortex flow (\circ) and the shear-band flow (\square). Error bars indicate statistical variation as described in the main text; for some data, the error bars are smaller than the plot symbols.

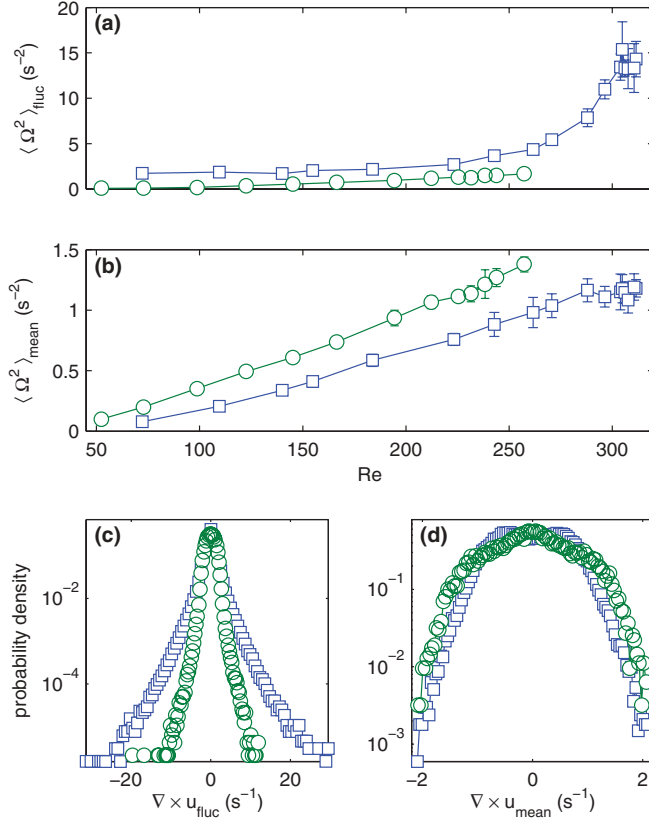


FIG. 4. (Color online) Average enstrophy (Ω^2) for the (a) fluctuating and (b) mean components of the flow field. Data are shown for the vortex flow (\circ) and the shear-band flow (\square). Probability density functions of the (c) fluctuating and (d) mean vorticity are also shown. The distributions come from experiments with $\text{Re} = 243$ (shear-band flow) and $\text{Re} = 244$ (vortex flow). Error bars indicate statistical variation as described in the main text; for some data, the error bars are smaller than the plot symbols.

In Fig. 4, we show results for the vorticity $\omega = \nabla \times \mathbf{u}$ and enstrophy $\Omega^2 = |\nabla \times \mathbf{u}|^2/2$ in the two flows. We find, perhaps counter-intuitively, that the vortex flow produces less fluctuating enstrophy than the shear-band flow does, although (unsurprisingly) there is more enstrophy in the mean component of the vortex flow. As shown in Figs. 4(c) and 4(d), where we plot the probability density functions of vorticity for the two flows at a fixed Re , the shear-band flow also shows an enhanced likelihood of very large fluctuations of vorticity relative to the vortex flow. Thus, it seems that the shear-band flow drives more intense velocity gradients than the vortex flow does.

Our conclusions drawn from the vorticity data are supported by measurements of the rate of strain $S_{ij} = (\partial_i u_j + \partial_j u_i)/2$, shown in Fig. 5. We find that, similar to the vorticity, the shear-band flow produces stronger fluctuating strain and less mean strain than the vortex flow. Thus, we find that the shear-band forcing leads to a flow with strong fluctuating velocity gradients, while the vortex-lattice forcing creates a flow with more turbulent kinetic energy. Let us also note that measurements of the velocity increments show nearly no differences between the two flows.

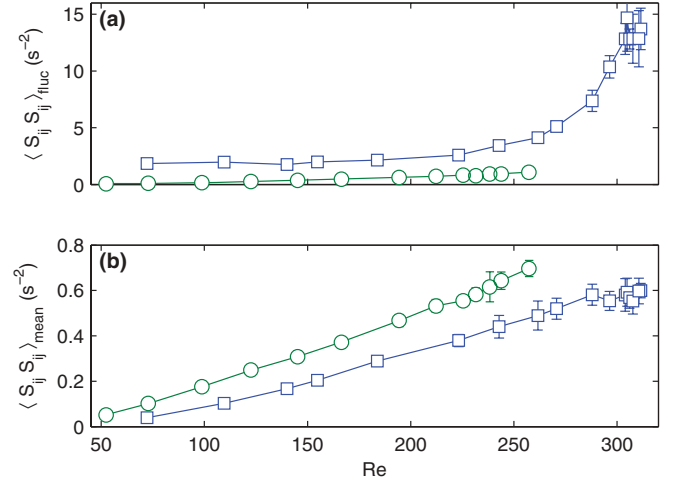


FIG. 5. (Color online) Average squared strain rate $\langle S_{ij} S_{ij} \rangle$, where summation is implied over repeated indices, for the (a) fluctuating and (b) mean components of the flow field. Data are shown for the vortex flow (\circ) and the shear-band flow (\square). Error bars indicate statistical variation as described in the main text; for some data, the error bars are smaller than the plot symbols.

C. Spectral fluxes

To understand these results in more detail, we turn to a spectral description of these flows to characterize how energy is driven away from the injection scale. Rather than taking a fully spectral approach by calculating, for example, energy spectra, we instead turn to the recently developed tool of so-called filter-space techniques (FSTs) that allow the direct measurement of spectral energy fluxes [19–25]. We have previously applied FSTs to this flow and studied their Lagrangian properties [26].

The idea of an FST is simple, and relies on *a posteriori* low-pass filtering of the velocity. Let $u_i^{(L)}$ be the i th component of the velocity field filtered at spatial scale L , so that spatial variation on scales smaller than L is suppressed. The equation of motion for the filtered kinetic energy $E^{(L)} = [u^{(L)}]^2/2$ can then be written as [20]

$$\frac{\partial E^{(L)}}{\partial t} = -\frac{\partial J_i^{(L)}}{\partial x_i} - \nu \frac{\partial u_i^{(L)}}{\partial x_j} \frac{\partial u_i^{(L)}}{\partial x_j} - \Pi^{(L)}, \quad (7)$$

where summation is implied over repeated indices. The first term on the right-hand side of Eq. (7) is the divergence of a spatial flux $J_i^{(L)}$, and acts to move energy in space. The second term represents the direct dissipation of (filtered) energy by viscous effects. Both are directly analogous to terms that appear in the equation of motion for the full (unfiltered) kinetic energy. The last term, however, has no analog and accounts for the coupling of the resolved scales to the filtered scales, and thus the spectral flux of energy between scales smaller than L and scales larger than L . It is given by

$$\Pi^{(L)} = -[(u_i u_j)^{(L)} - u_i^{(L)} u_j^{(L)}] \frac{\partial u_i^{(L)}}{\partial x_j}. \quad (8)$$

Defined this way, $\Pi^{(L)} > 0$ denotes transfer to smaller scales, and $\Pi^{(L)} < 0$ denotes transfer to larger scales. We use a Gaussian low-pass filter to implement the FST [26].

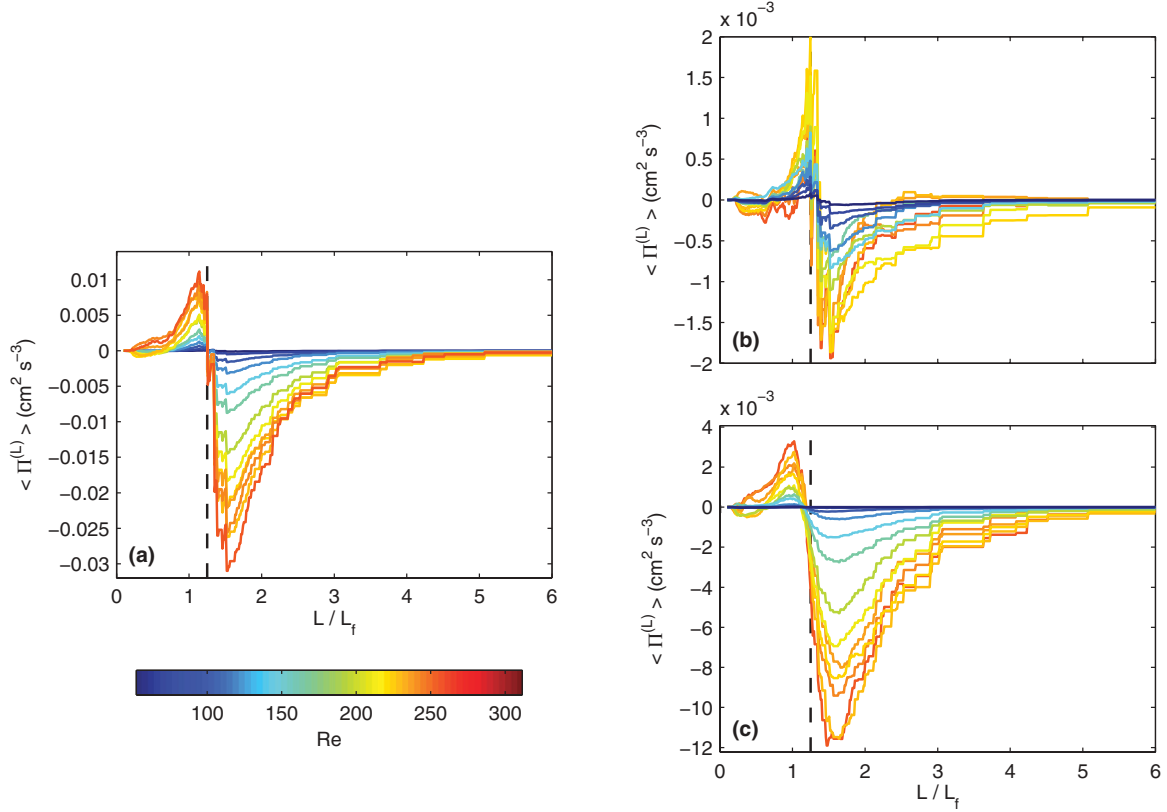


FIG. 6. (Color online) Mean spectral energy flux $\langle \Pi^{(L)} \rangle$ in the vortex flow for (a) the entire flow field, (b) the mean flow, and (c) the fluctuations. The different curves are for different Reynolds numbers, as indicated by the color bar. The scale at which $\langle \Pi^{(L)} \rangle = 0$ in the entire flow, which we define as the energy crossover scale, is indicated by a dashed line in all three panels.

In Fig. 6(a), we show the mean spectral energy flux $\langle \Pi^{(L)} \rangle$, computed for the whole flow field over a range of Reynolds numbers, as a function of filter scale L for the vortex flow. For all Reynolds numbers, the $\langle \Pi^{(L)} \rangle$ curves cross zero at the same length scale $L_c \approx 1.25 L_f$, as one would expect given that the length scale of the forcing is fixed by the geometry of the apparatus. We refer to L_c as the energy crossover scale, and note that it gives the effective energy injection scale for the system. For $L > L_c$, energy is driven to larger length scales (negative energy flux), in a nascent inverse energy cascade. For $L < L_c$, we observe a (weaker) transfer of energy to smaller scales.

We also computed the spectral energy flux for the mean flow and the fluctuations, shown in Figs. 6(b) and 6(c). The mean flow shows much weaker spectral flux than the whole flow (note the different vertical scale), as one would expect given that the mean flow is by definition stationary and locked to the forcing geometry. Note that the forward and reverse transfer peaks are of similar magnitude. The spectral-flux curves computed from the fluctuating velocities are much more similar in size and shape to those of the whole flow. We note that the energy crossover scale L_c measured from the fluctuating velocities is slightly different (roughly 6% smaller) from the value computed for the whole flow. Thus, even though the magnet spacing L_f is set by the geometry of the apparatus, the energy crossover scale is a dynamical parameter and is not fixed. We do find, however, that L_c remains constant as a function of Reynolds number. Finally, let us note that the mean energy flux measured for the *total* flow field is not given by

the sum of the fluxes measured from the mean and fluctuating components separately. This mismatch is due to the appearance of coupling terms in the spectral flux equations between the mean and fluctuating parts of the flow field.

The spectral energy flux computed from the shear-band flow, shown in Fig. 7, has features that are qualitatively similar to the vortex flow. We again find that the energy crossover scale L_c is constant as a function of Reynolds number. Its value, however, is somewhat different, even though the magnet spacing is unchanged. We find that $L_c \approx 1.75 L_f$ for the whole flow; a second minimum in $|\langle \Pi^{(L)} \rangle|$ is also apparent for all Reynolds numbers at approximately $2L_f$, corresponding to the full wavelength of the shear bands. Above this scale, we again see inverse energy transfer, while we find forward transfer for $L < L_c$. The spectral energy flux computed for only the mean flow field is also similar to the vortex flow, though again with a different energy crossover scale. The mean flow shows $\langle \Pi^{(L)} \rangle > 0$ for scales smaller than the crossover scale and appears to carry the majority of the forward energy flux.

The spectral energy flux computed from the fluctuating component of the shear-band flow, however, is qualitatively different from the vortex flow. First, we find that $\langle \Pi^{(L)} \rangle < 0$ for all scales, even for $L < L_c$. Although this behavior is expected for $L > L_c$, it is surprising for $L < L_c$. $\langle \Pi^{(L)} \rangle < 0$ for $L < L_c$ implies some small-scale source of fluctuating kinetic energy. The nature of this source is at present unclear: it might be due to a weak small-scale energy source due to instabilities of the shear-band forcing or with coupling between the fluctuating

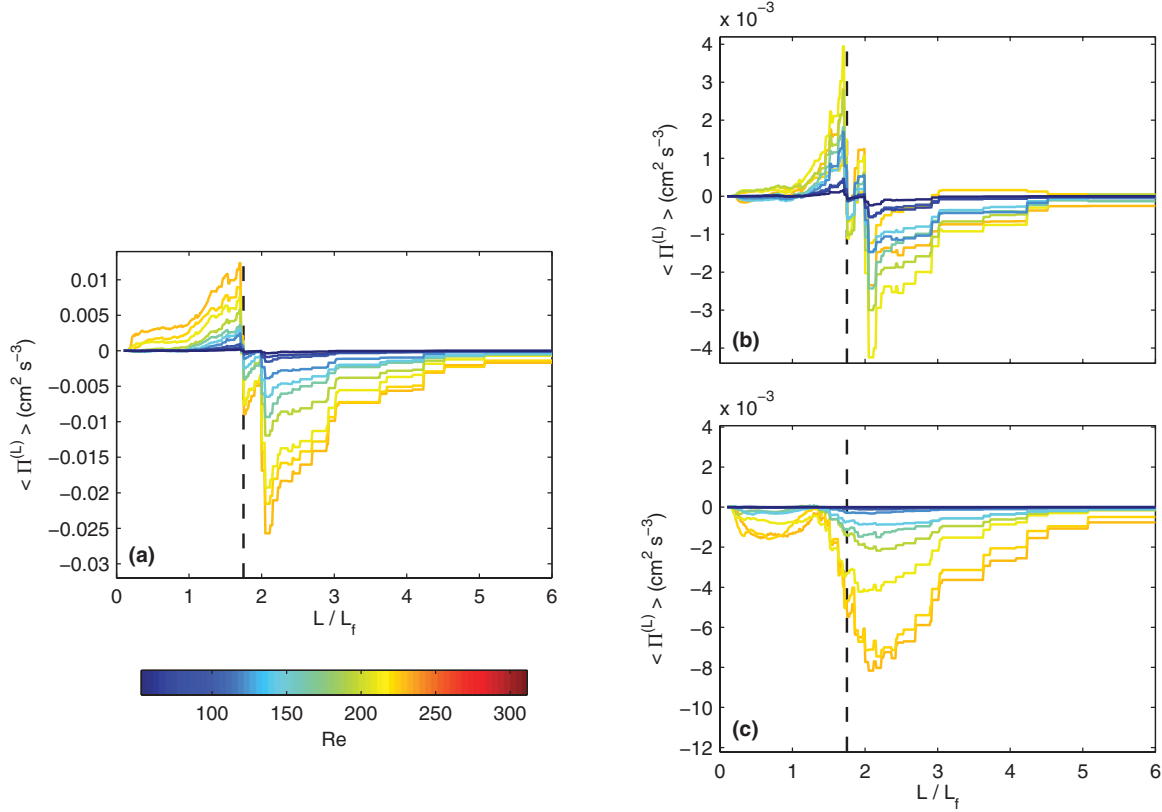


FIG. 7. (Color online) Mean spectral energy flux $\langle \Pi^{(L)} \rangle$ in the shear-band flow for (a) the entire flow field, (b) the mean flow, and (c) the fluctuations. The different curves are for different Reynolds numbers, as indicated by the color bar (which matches the color bar in Fig. 6). The energy crossover scale is indicated by a dashed line in all three panels.

and mean components of the flow. We leave its detailed investigation for future work. We also find that the energy crossover scale for the fluctuations is much smaller (nearly 25%) than it is for the whole flow, a variation that is much larger than it is for the vortex flow. Thus, the dominant *dynamical* length scale in the shear-band flow is smaller compared to its value for the whole flow than it is for the vortex flow.

D. Discussion

To summarize our findings, we find that the vortex flow shows more fluctuating kinetic energy but weaker fluctuating gradients than the shear-band flow over a similar range of forcing strengths. The dynamical energy crossover scale L_c varies only slightly between the fluctuating field and the whole flow for the vortex lattice, while the difference is much larger for the shear-band flow, with L_c for the fluctuations almost 25% smaller than it is for the whole flow.

To explain these differences, we first consider the forcing symmetries of the two flows. The checkerboard magnet arrangement of the vortex flow has a discrete translational symmetry in both the \hat{x} and \hat{y} directions. Thus, the flow is highly constrained by the forcing, and fluctuations are not completely free to develop except at very high Reynolds numbers; the flow tends to lock onto the magnet lattice quite strongly for this arrangement [27]. The situation is different for the shear-band flow. In this case, the flow is free to develop

along the shear bands, allowing the production of smaller length scales and thus larger velocity gradients.

Our measurements of the spectral energy fluxes also shed light on why the vortex lattice shows more kinetic energy while the shear-band flow shows stronger gradients. At any individual Reynolds number, the *total* amount of energy injected into the flow is the same for both geometries, given how we have defined the Reynolds number, but the energy crossover scale L_c is measured to be larger for the shear-band flow. Thus, it is reasonable to hypothesize that more of the injected energy flows to smaller scales in the shear-band flow, where it drives small-scale motion and therefore larger gradients. More of this energy, however, is directly dissipated by small-scale viscous effects. Further study will be required to understand the detailed implications of our finding that the mean energy flux due to the fluctuating component of the velocity field is always negative for the shear-band flow. In contrast, the vortex flow drives most of its injected energy to larger scales via an inverse cascade. At these larger scales, viscous forces are weak, and thus more kinetic energy persists in the flow field, since the large-scale friction in our flow is also weak. On the other hand, the velocity gradients associated with these larger scales are smaller, leading to the phenomena we observe.

IV. SUMMARY AND CONCLUSIONS

We have studied the statistics of the weak turbulence produced in a thin electromagnetically stirred fluid layer under

two different forcing configurations: a checkerboard lattice of magnets that produces a steady vortex flow at low Reynolds number and stripes of magnets that produce steady shear bands. We showed that the geometry of the forcing has measurable consequences. The vortex flow leads to more fluctuating kinetic energy, while the shear-band flow drives stronger gradients. These results can be explained by considering the symmetries of the forcing and the spectral transfer of energy.

Our results show that the geometry of the forcing is a non-negligible factor in determining the dynamics of the flow field,

since the Reynolds number in this type of apparatus must be kept low to avoid three-dimensional secondary flows [7] and thus an asymptotic regime independent of forcing cannot be reached. Thus, we suggest that the forcing can be chosen in experiments to optimize the effects of interest (for example, strong large-scale motion or large velocity gradients).

ACKNOWLEDGMENT

This work was supported by the US National Science Foundation under Grant No. DMR-0906245.

-
- [1] R. H. Kraichnan and D. Montgomery, *Rep. Prog. Phys.* **43**, 547 (1980).
 - [2] G. Boffetta and R. E. Ecke, *Annu. Rev. Fluid Mech.* **44**, 427 (2012).
 - [3] D. B. Blum, G. P. Bewley, E. Bodenschatz, M. Gibert, A. Gylfason, L. Mydlarski, G. A. Voth, H. Xu, and P. K. Yeung, *New J. Phys.* **13**, 113020 (2011).
 - [4] R. H. Kraichnan, *Phys. Fluids* **10**, 1417 (1967).
 - [5] C. E. Leith, *Phys. Fluids* **11**, 671 (1967).
 - [6] G. K. Batchelor, *Phys. Fluids* **12**, II-233 (1969).
 - [7] D. H. Kelley and N. T. Ouellette, *Phys. Fluids* **23**, 045103 (2011).
 - [8] P. Tabeling, S. Burkhart, O. Cardoso, and H. Willaime, *Phys. Rev. Lett.* **67**, 3772 (1991).
 - [9] D. Rothstein, E. Henry, and J. P. Gollub, *Nature* **401**, 770 (1999).
 - [10] H. J. H. Clercx, G. J. F. van Heijst, and M. L. Zoetewij, *Phys. Rev. E* **67**, 066303 (2003).
 - [11] M. K. Rivera and R. E. Ecke, *Phys. Rev. Lett.* **95**, 194503 (2005).
 - [12] L. Rossi, J. C. Vassilicos, and Y. Hardalupas, *J. Fluid Mech.* **558**, 207 (2006).
 - [13] H. Xia, D. Byrne, G. Falkovich, and M. Shats, *Nat. Phys.* **7**, 321 (2011).
 - [14] D. H. Kelley and N. T. Ouellette, *Am. J. Phys.* **79**, 267 (2011).
 - [15] N. T. Ouellette, H. Xu, and E. Bodenschatz, *Exp. Fluids* **40**, 301 (2006).
 - [16] N. Mordant, A. M. Crawford, and E. Bodenschatz, *Physica D* **193**, 245 (2004).
 - [17] T. P. Sapsis, N. T. Ouellette, J. P. Gollub, and G. Haller, *Phys. Fluids* **23**, 093304 (2011).
 - [18] P. Lynch, *Mon. Weather Rev.* **117**, 1492 (1989).
 - [19] M. Germano, *J. Fluid Mech.* **238**, 325 (1992).
 - [20] G. L. Eyink, *J. Stat. Phys.* **78**, 335 (1995).
 - [21] M. K. Rivera, W. B. Daniel, S. Y. Chen, and R. E. Ecke, *Phys. Rev. Lett.* **90**, 104502 (2003).
 - [22] S. Chen, R. E. Ecke, G. L. Eyink, X. Wang, and Z. Xiao, *Phys. Rev. Lett.* **91**, 214501 (2003).
 - [23] S. Chen, R. E. Ecke, G. L. Eyink, M. Rivera, M. Wan, and Z. Xiao, *Phys. Rev. Lett.* **96**, 084502 (2006).
 - [24] Z. Xiao, M. Wan, S. Chen, and G. L. Eyink, *J. Fluid Mech.* **619**, 1 (2009).
 - [25] M. Wan, Z. Xiao, C. Meneveau, G. L. Eyink, and S. Chen, *Phys. Fluids* **22**, 061702 (2010).
 - [26] D. H. Kelley and N. T. Ouellette, *Phys. Fluids* **23**, 115101 (2011).
 - [27] N. T. Ouellette and J. P. Gollub, *Phys. Fluids* **20**, 064104 (2008).